Experimental and numerical investigation on the hydroelastic response of barge and KVLCC2 ship

Xie, Binyang; He, Guanghua; Zhao, Chuankai; Jing, Penglin; Kumar Pal, Sumit; Iijima, Kazuhiro; Jin, Ruijia; Chen, Bangqi; Ghassemi, Hassan

DOI
10.1016/j.oceaneng.2024.118081

Publication date
2024

Document Version
Final published version

Published in
Ocean Engineering

Citation (APA)
Xie, B., He, G., Zhao, C., Jing, P., Kumar Pal, S., Iijima, K., Jin, R., Chen, B., & Ghassemi, H. (2024). Experimental and numerical investigation on the hydroelastic response of barge and KVLCC2 ship. *Ocean Engineering*, *307*, Article 118081. https://doi.org/10.1016/j.oceaneng.2024.118081

Ocean Engineering 307 (2024) 118081

Contents lists available at ScienceDirect

Ocean Engineering

journal homepage: www.elsevier.com/locate/oceaneng

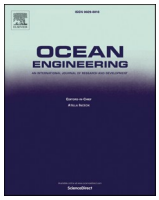

Research paper

Experimental and numerical investigation on the hydroelastic response of barge and KVLCC2 ship

Binyang Xie [b], Guanghua He [a,*], Chuankai Zhao [a], Penglin Jing [a], Sumit Kumar Pal [c], Kazuhiro Iijima [b], Ruijia Jin [d], Bangqi Chen [a], Hassan Ghassemi [a]

[a] Department of Naval Architecture and Ocean Engineering, Harbin Institute of Technology, Weihai, China
[b] Department of Naval Architecture and Ocean Engineering, Osaka University, Osaka, Japan
[c] Department of Aerospace Engineering, Delft University of Technology, Kluyverweg 1, 2629 HS, Delft, Netherlands
[d] Tianjin Research Institute for Water Transport Engineering, M.O.T., Tianjin, 300456, China

ARTICLE INFO

Keywords:
Segmented barge ship
KVLCC2 ship
Hydroelastic response
CFD-FEA coupled method

ABSTRACT

In this paper, the hydroelasticity of two segmented ship models (Barge and KVLCC2) is investigated by experimental and numerical methods. A two-way Computational Fluid Dynamics (CFD) and Finite Element Analysis (FEA) coupled method is adopted and further validated its accuracy against experimental results. The current approach emphasizes the overall convergence between two solvers, maintaining a strongly coupled manner to comprehensively address the fluid-structure interaction phenomenon, including the added mass effect. A series of experiments of a segmented Barge and KVLCC2 under various wave conditions were firstly conducted. The motions of the models are measured and the displacement Response Amplitude Operators (RAOs) are calculated. The CFD-FEA coupled method is demonstrated in agreement with experimental results by comparing the numerical prediction with the tank test results in terms of motion, affirming the validity and robustness. Finally, the hydroelastic response is discussed and investigated.

1. Introduction

In the traditional design procedure, analysis of wave-induced motion and load responses are generally based on rigid ship. Structure-response analysis is performed separately using empirical formulas or the frequency-domain analysis method. The increase in ship size has made it challenging to evaluate the safety of ship structures using traditional analysis methods, particularly when ships encounter complex sea conditions. The enlargement of a ship's size can result in a decrease in its natural frequency, making it more vulnerable to whipping and springing (Lee et al., 2011; Southall et al., 2015). When ships with a low natural frequency interact with incoming waves, resonance is more likely to occur, which can cause local deformation or even structural failure. The hydroelastic response at a global level can apparently affect both the extreme structural response and the fatigue life of certain structural details (Malenica et al., 2006). For instance, the maritime accident involving the MOL Comfort has two possible causes (Class NK, 2014). The structural response of the ship will increase as the combination of global and local loads as well as the hydroelastic vibration. Therefore, when predicting the safety and motion response of large ships, it is essential to consider Fluid-Structure Interaction (FSI) and the elasticity of the structure, also known as hydroelasticity. The analysis considering hydroelasticity offers several advantages (Wu and Tian, 2008).

(1) Compared with traditional seakeeping analysis, information from the fluid field can be made the best of. Thus, while predicting the rigid body motion, the results of deformation, strain, stress, bending moment, and shear force of structure, can be given;
(2) A precise phase relationship between the steady wave induced load and the transient slamming load of the ship can be given when sailing in waves;
(3) Ship structure response from global and local hydrodynamic loads can be integrated and investigated naturally;
(4) When sailing in waves, the structure strength, dynamic stability and fatigue performance of the ship hull can be unified and studied together. This can lay a foundation for direct ship-design methods.

* Corresponding author.
E-mail address: ghhe@hitwh.edu.cn (G. He).

https://doi.org/10.1016/j.oceaneng.2024.118081
Received 2 February 2024; Received in revised form 22 April 2024; Accepted 1 May 2024
Available online 14 May 2024

In the 1970th, Bishop et al. developed a two-dimensional linear hydroelasticity theory (Bishop and Price, 1979, 1983) to address the interaction problem between elastic beams and fluids. This theory laid the foundation for the branch of hydroelasticity. Later, the emergence and popularisation of high-performance computers lead to the development of three-dimensional hydrodynamic methods for solving hydroelasticity problems. Wu (1984) proposed a three-dimensional linear hydroelasticity theory that considers generalized fluid-structure coupling boundary conditions. The theory can estimate the motion response of any elastic body in waves. Price (1985) introduced an approximate correction to Wu's theory for fluid viscous resistance, allowing for analysis of its influence. Wu's theory was validated through a series of examples and further improved by Bishop et al. (1986). However, linear hydroelasticity theory assumes small disturbances of the fluid and minimal displacement and deformation of the structure. This assumption is not always applicable. Therefore, nonlinear hydroelasticity theory was further developed (Chen et al., 2003; Korobkin et al., 2011; Lee and Lee, 2016; Xia et al., 1998). Consideration has been given to factors such as the instantaneous change of structure immersion depth, anharmonic oscillation, and the slamming effect of waves. However, analytical solutions alone may not suffice for complicated hydroelastic problems. There are two primary methods for experimental study of hydroelasticity: real-ship test and model test. Results from real-ship tests are precise. However, conducting such tests is generally expensive and challenging. Due to the scale effect, there is a discrepancy between the results obtained from the model test and the actual results. The model test can meet the basic requirements for general design and construction and is therefore widely used. Riggs et al. (2007) proposed two simple ship models called Barge and Wigley, which have become the benchmarks of three-dimensional hydroelasticity studies. Senjanović and Malenica (2003) conducted a tank test on a segmented Barge ship to study the hydroelasticity under regular waves. Remy et al. (2006) investigated the elastic response of a Barge ship to diagonal waves, based on Malenica's experiment. Fu et al. (2007) investigated the general characteristics of hydroelastic response in flexible floating interconnected structures, including their displacement and bending moments under various conditions. Iijima et al. (2009) and Zhu et al. (2011a, 2011b) designed scaled ship models based on real ships. The study focused on the wave frequency response, bending and torsional vibrations of the segmented ship model in both regular and irregular waves. Chen et al. (2017) investigated the vibration characteristics of a segmented ship model at varying wave angles. Fonseca and Guedes Soares (2004) conducted a model test on a S-175 container ship. The results reveal the non-linear response of the structure. A self-propelled test of a segmented ship was conducted by Jiao et al. (2018). Kim et al. (2018) investigated fatigue damage in a 9400 Transmission Extension Unit (TEU) container ship based on a real ship test. Yang et al. (2021) conducted a large-scale combined beam model experiment on a 20,000TEU container ship. Jiao et al. (2019) investigated hydroelastic responses through a model experiment in harsh irregular seaways.

Numerical simulation has become the most effective and economical solution for studying hydroelasticity in recent years. Guo and Zou (2017) investigated ship maneuvering with four degrees of freedom (DOF) in still water using the ONR roll ship model. Iijima et al. (2008) proposed a consistent structural analysis procedure to estimate the global and local load effects considering symmetric and antisymmetric hydroelastic vibrations in high waves. Kim et al. (2009) investigated torsion, bending and warping distortion of a one-dimensional beam using a hybrid Boundary Element Method (BEM)-FEM scheme. He and Kashiwagi (2012) investigated the hydroelastic response of an elastic vertical plate under solitary waves using a BEM-FEM coupled method. Takami et al. (2018, 2020) developed an inhouse code and conducted one-way and two-way CFD-FEA coupled simulation for hydroelastic response using an Inverse Distance Weighting (IDW) mapping algorithm (Nishikawa, 2012). This in-house code can couple any CFD and FEA code, providing a new option for investigating hydroelasticity. Jiao et al. (2021) and Huang et al. (2022) estimated ship wave loads and hydroelastic responses using fully coupled computational fluid dynamics (CFD) and finite element analysis (FEA) solvers in a two-way manner, with Star-CCM+ and Abaqus, respectively. Pal and Iijima (2022) attempted to investigate the higher-order springing phenomenon using direct coupling of CFD-FEM analysis for a barge-type structure. Pal et al. (2023) investigated the hull girder collapse behavior in the case of a 5250 TEU containership using a coupling between CFD and FEA. Lu et al. (2024) analyzed the structural collapsed characteristics of a three-cabin structure using CFD-FEA coupled method. The fully coupled CFD-Discrete Module Beam (DMB) method is also developed and used for ship hydroelasticity (Wei et al., 2023) and Very Large Floating Structures (VLFS) (Wei et al., 2024) recently.

The objectives of the present study could be summarized as follows.

1. Tank tests were conducted on the segmented Barge and KVLCC2 models under various wave conditions. The motion was measured, and the hydroelasticity of the models was focused.
2. Experimental analysis and two-way CFD-FEA coupled method in this research were validated by published data.

2. Tank test

2.1. Ship model

This study employed two segmented ship models, namely Barge and KVLCC2, as shown Fig. 1. Experiment on the Barge ship is based on the experiment carried out by Senjanović and Malenica (2003), while the experiment on the KVLCC2 ship is newly designed based on the model and data provided by Zhang et al. (2019).

In the Barge model, there are a total of twelve segments rigidly connected to the backbone, as shown in Fig. 2. Apart from the bow segment (refer to Fig. 3), the remaining eleven segments are identical in shape. The gap between each segment is set at 0.015 m. Table 1 describes the principal particulars of the Barge ship.

Regarding the KVCLL2 model, it is divided into sixteen segments due to the complexity of ship lines and the rapid changes in curvature of the ship's surface (see Fig. 1 (b)). Compared to the original ship, the

(a) Barge

(b) KVLCC2

Fig. 1. Experimental ship model.

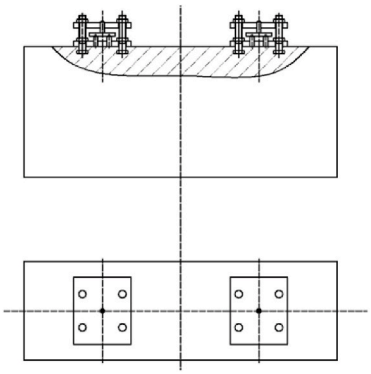

Fig. 2. Connection between segment and backbone.

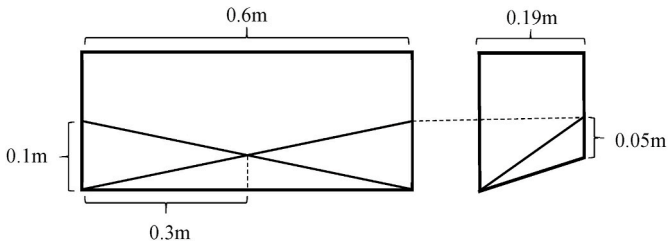

Fig. 3. Bow segment of the Barge ship.

Table 1
Principal particulars of the Barge ship model.

	Length (m)	Width (m)	Depth/Thickness (m)	Draft (m)
Segment	0.190	0.600	0.250	0.120
Backbone beam	2.445	0.050	0.006	/

experimental model's deck has been raised to prevent green water from entering during the experiment. Similar to the Barge model, all the segments are rigidly connected to the backbone. The distance between each segment is 0.013 m. The length of F2 to F7 and F10 to F11 is 0.15 m, while the length of F8 and F9 is 0.18 m. To ensure the accuracy of the lines in the bow and stern, F1 and F16 were created by 3D printing technology (see Fig. 4). The backbone of the model measures 2.729 m in length, 0.1 m in width and 0.005 m in thickness. The principal particulars of the KVLCC2 ship model are listed in Table 2.

Fig. 5 shows the mass distribution of the Barge and KVLCC2 models along the *x*-axis. In the Barge model, all segments are box-type and have a similar size, resulting in a similar weight for each segment. The KVLCC2 model's mass distribution is based on the actual ship, with the weight of each segment decreasing from the center to the two ends, as depicted in Fig. 5 (b).

(a) Bow (b) Stern

Fig. 4. The bow and stern segments of the KVLCC2 model.

Table 2
Principal particulars of the KVLCC2 ship model.

	Length (m)	Width (m)	Depth (m)	Draft (m)	Center of gravity (m)
Symbol	L_{pp}	B	D	d	KG
Value	2.728	0.486	0.2917	0.2117	0.155

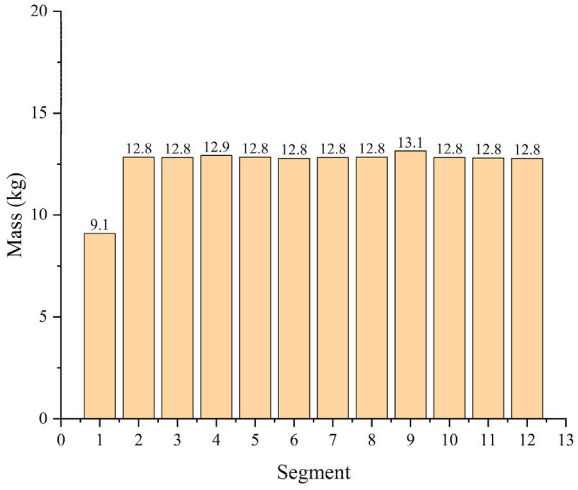

(a) Barge

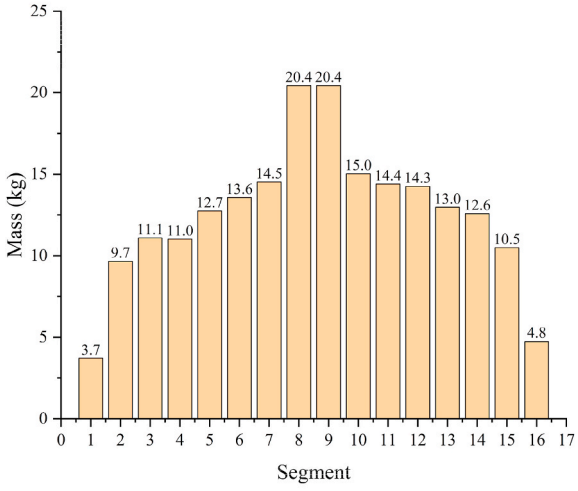

(b) KVLCC2

Fig. 5. Mass distribution of the Barge ship and KVLCC2 ship.

2.2. Mooring system

In the experiment, the ship model is constrained by spring to avoid unexpected motion (see Fig. 6). Only heave and pitch are released.

2.3. Motion capture system

As shown in Fig. 8, a VISUALEYES™ 3D motion capture system, which includes a tracker and several wireless LED markers, was adopted in the experiment. The tracker captures real-time signals from multiple LED markers and computes motion with high accuracy. The location of the LED markers for Barge and KVLCC2 is shown in Fig. 7. The motion

Fig. 6. Spring mooring system.

capture system measures the displacement along the z direction at each LED marker.

2.4. Wave tank and wave conditions

The tank test was carried out in the wave tank at the Tianjin Research Institute for Water Transport Engineering (TIWTE). The wave tank is 40 m in length, 12 m in width and 0.9 m in depth. A piston wave maker is adopted and plenty of wave eliminators are settled at the side of the tank, behind the wave maker and by the end of the tank to avoid wave reflection.

In this research, the ship under different regular waves without forward speed is investigated. The wave conditions of the experiment are shown in Table 3. The wave period for all test conditions is determined by the sea conditions in the northern hemisphere (Bales, 1983).

3. Numerical theory and model

3.1. FE formulation and model

3.1.1. FE formulation

An implicit solution is adopted in the FEA calculation phase. For the dynamic problem, the linearized equilibrium equations can be written by:

$$M\ddot{U} + C\dot{U} + KU = R \tag{1}$$

where M, C and K represent the mass matrix, damping matrix, and stiffness matrix, respectively; R is the external load vector; U, $\dot{U}$ and $\ddot{U}$ respectively represent displacement, velocity and acceleration vector of FEA nodes.

As for time integration, the Newmark-β method (Newmark, 1959) is applied in the FEA calculation phase, which can be written as:

$$\begin{cases} \ddot{U}^{t+1} = \dfrac{\Delta U}{\beta \Delta t^2} - \dfrac{\dot{U}^t}{\beta \Delta t} - \dfrac{1}{\beta}\left(\dfrac{1}{2} - \beta\right)\ddot{U}^t \\ \dot{U}^{t+1} = \dot{U}^t + \Delta t(1\text{-}\gamma)\ddot{U}^t + \gamma \Delta t \ddot{U}^{t+1} \end{cases} \tag{2}$$

where the superscript t and $t+1$ represent value at time step t and $t+1$; Δt is the time step; β and γ are time integral constants. Since the Newmark method lacks the robustness required for simulating long-term dynamic implicit problems, a three-point backward Euler step is introduced between two Newmark steps, which can be written as:

$$\begin{cases} \ddot{U}^{t+1} = \dfrac{(1+\alpha)}{\Delta t}\left(\dot{U}^{t+1}\text{-}\dot{U}^t\right) - \dfrac{\alpha}{\Delta t_n}\left(\dot{U}^t - \dot{U}^{t\text{-}1}\right) \\ \dot{U}^{t+1} = \dfrac{(1+\alpha)}{\Delta t}\Delta U - \dfrac{\alpha}{\Delta t_n}\left(U^t - U^{t\text{-}1}\right) \end{cases} \tag{3}$$

where Δt_n represents time step at the pre-Newmark time step; α is the time integral constant. For these time integral constants, the Bath scheme (see Table 4) is reported to preserve energy and momentum to a reasonable degree (Bathe, 2007). If necessary, the time integral constant should be adjusted based on the Bath scheme. Usually, increasing the value of β and γ can bring additional numerical damping, which will increase the stability of the simulation. In this study, the settings of time integral constants are shown in Table 4. Rayleigh-type damping is applied to the FE model. Both mass damping and stiffness damping are considered in the simulation. The mass damping and stiffness damping coefficients are set to 0.01 and 0.001, respectively. Since the stiffness proportional damping constant largely affects the high-frequency mode of structure (Bathe and Noh, 2012), the unstable calculation can be caused by taking the stiffness damping into account. The time step size should be forced to a significantly small value in this kind of case. Therefore, the time step size for the FEA solver is set to 10^{-5}s in this

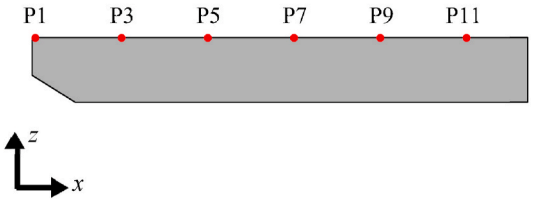

Monitor	Location along x-axis (m)
P1	0
P3	0.41
P5	0.82
P7	1.22
P9	1.64
P11	2.05

(a) Barge

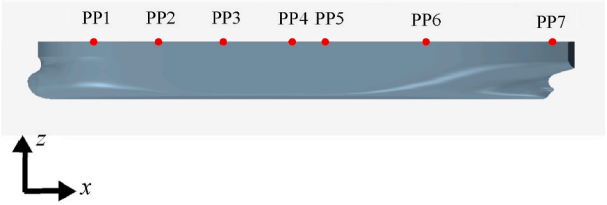

Monitor	Location along x-axis (m)
PP1	0.25
PP2	0.58
PP3	0.90
PP4	1.27
PP5	1.45
PP6	1.94
PP7	2.59

(b) KVLCC2

Fig. 7. Location of the LED markers.

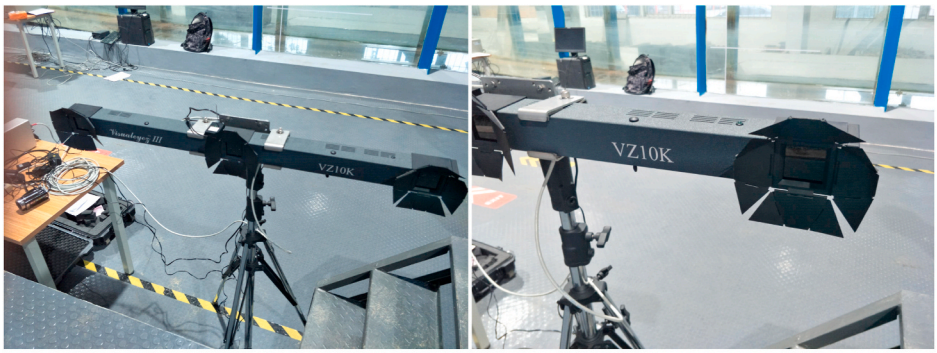

(a) Tracker

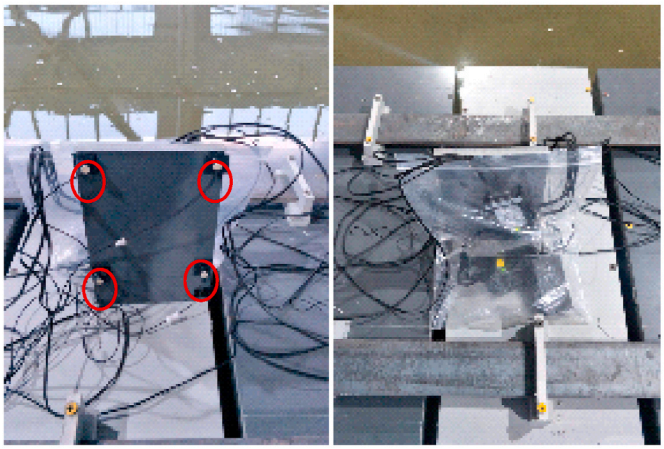

(b) Wireless LED marker

Fig. 8. Motion capture system.

Table 3
Wave condition.

Wave Condition	Wave height h_0 (m)	Wave period t_0 (s)	Wavelength λ (m)
EX-A1	0.100	1.6	3.996
EX-A2	0.100	1.4	3.063
EX-A3	0.100	1.2	2.248
EX-A4	0.100	1.0	1.561
EX-C3	0.100	1.100–1.850	1.889–5.342
EX-C4	0.070	1.100–1.850	1.889–5.342
EX-C5	0.045	1.100–1.850	1.889–5.342
EX-C6	0.030	1.100–1.850	1.889–5.342

Table 4
FEA time integration setting.

Parameter	In this study	Bath scheme
α	0.5	0.5
β	0.4	0.25
γ	0.6	0.5
time step	10^{-5}s	/

study.

3.1.2. FE model

The FE model of the Barge ship and KVLCC2 ship are shown in Fig. 9. The FE model of the Barge ship is the same as the experimental model, which is segmented. It should be noted that the FE model of the KVLCC2 ship is continuous and does not have backbone. In the experiment of the KVLCC2 ship, contact between two neighbor segments was observed. Accounting for this kind of contact in current two-way coupled methods is time-consuming. Furthermore, due to the narrow gap between neighbor segments and the complex geometry of the ship, it is necessary to ensure high mesh quality in the CFD simulation and use a smaller time step for the two-way coupled simulation. Therefore, to balance accuracy and efficiency in the simulation, a continuous FE model has been adopted for the KVLCC2 ship.

Young's modulus of the ship is tuned to reduce the stiffness of the FE model to a reasonable level. Material characteristics of the backbone are shown in Table 5. The numerical models are divided into 12 (Barge ship) and 16 parts (KVLCC2 ship) respectively to ensure that the mass distribution is as same as the experiment models. Translation along the x and z axes, as well as rotation along the x and y axes, is constrained at the center of the ship's mass. Only the heave and pitch of the ship are released in the simulation.

3.2. CFD model

The FEM implemented in a commercial incompressible CFD solver from LS-DYNA is applied in the CFD computation phase. The calculation setup of CFD is shown in Table 6. The incompressible Navier-Stokes equations could be written as:

$$\frac{\partial u}{\partial t} + \nabla \cdot (uu) = -\frac{1}{\rho}\nabla p + \nabla \cdot \left[\upsilon \nabla u + \upsilon (\nabla u)^T\right] \tag{4}$$

$$\nabla \cdot u = 0 \tag{5}$$

where ρ is the density of the fluid; u is the velocity of the fluid; p is the pressure; υ is the viscosity coefficient. Equations (4) and (5) represent the momentum equation and continuity equation, respectively. A three-

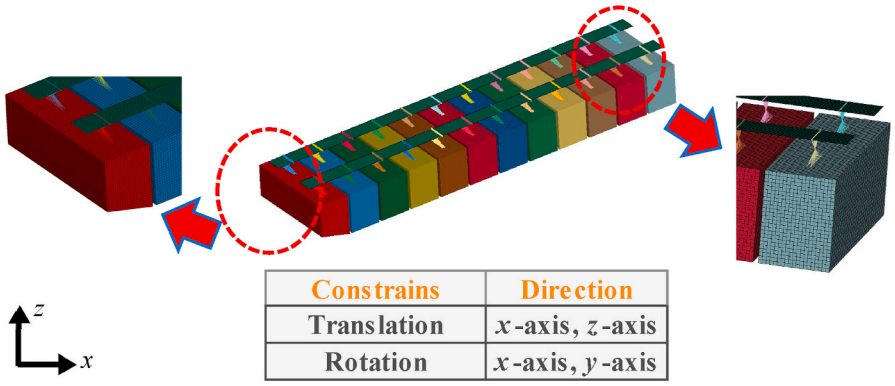

(a) Barge ship

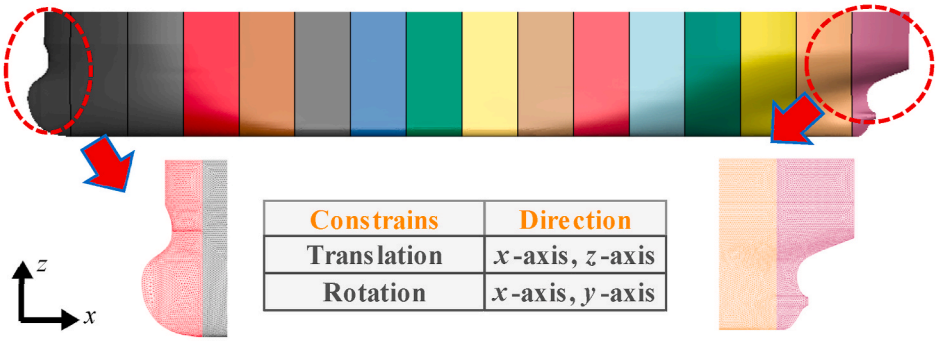

(b) KVLCC2 ship

Fig. 9. FE models of the Barge ship and KVLCC2 ship.

Table 5
Material characteristics.

Parameter	Barge	KVLCC2
Material properties	Elastic	Elastic
Young's modulus	6.0×10^{12}	1.4×10^{7}
Poisson's ratio	0.3	0.3

Table 6
Calculation setup of CFD.

Multiphase	Level set
Physical model of fluid	Incompressible
Solution	Unsteady implicit analysis
Turbulence model	Variational multiscale approach (VMS)

step fractional projection method is employed for the Navier-Stokes equations (Brown et al., 2001):

Step 1:

$$u_i^* - \mu \frac{dt}{\rho} \frac{\partial}{\partial x_j}\left(\frac{\partial u_i^*}{\partial x_j}\right) + u_j^* dt \frac{\partial \overline{u}_i^{n+1}}{\partial x_j} = u_i^n - \kappa \frac{dt}{\rho} \frac{\partial p^n}{\partial x_j} \delta_{ij} \tag{6}$$

Step 2:

$$\frac{\partial}{\partial x_i}\left(-u_i^*\right) = \frac{dt}{\rho} \frac{\partial}{\partial x_i} \frac{\partial}{\partial x_i}\left(-p^{n+1} + \kappa p^n\right) \delta_{ij} \tag{7}$$

Step 3:

$$u_i^{n+1} = u_i^* + \frac{dt}{\rho} \frac{\partial}{\partial x_j}\left(-p^{n+1} + \kappa p^n\right) \delta_{ij} \tag{8}$$

where u^* and u^{n+1} represent the predicted velocity and the final step divergence free velocity, respectively; dt is the time step size; κ is a scalar value that varies from 0 to 1, determining the amount of pressure splitting; δ_{ij} is the unit tensor; $\overline{u}^{n+1}$ is the estimation of u^{n+1}, which could be written as:

$$\overline{u}_i^{n+1} = 2u_i^n - u_i^{n-1} \tag{9}$$

In the first step, a predicted velocity u^* is computed. This velocity usually does not satisfy the incompressibility constrain given by Equation (5). Hence, in the second step, the velocity u^* is projected into a space of divergence free vector field and a Poisson equation of pressure is obtained. This pressure will correct u^* to get a final step divergence free velocity u^{n+1}. The final step consists of moving the FE nodes to their new time step position x^{n+1}. If this is done iteratively then convergence is achieved when the FE nodes always move to the same final position.

As shown in Fig. 10, the CFD solver uses a level set method (Osher, et al., 2004), a fast and reliable technique for accurately tracking and representing moving free surfaces. An implicit function φ whose zero isocontour ($\varphi = 0$) represents the interface is introduced, which could be defined as a distance function:

$$\varphi(x) = \begin{cases} \min\left(\left|x - x_{\text{interface}}\right|\right) \text{ on } \Omega^+ \\ 0 \text{ on} \partial\Omega \\ -\min\left(\left|x - x_{\text{interface}}\right|\right) \text{ on } \Omega^- \end{cases} \tag{10}$$

where x and $x_{\text{interface}}$ represent the coordinate of each CFD grid in the simulation domain and on the interface, respectively; Ω is the simulation domain. The fluid domain is defined by $\varphi > 0$, while the vacuum is

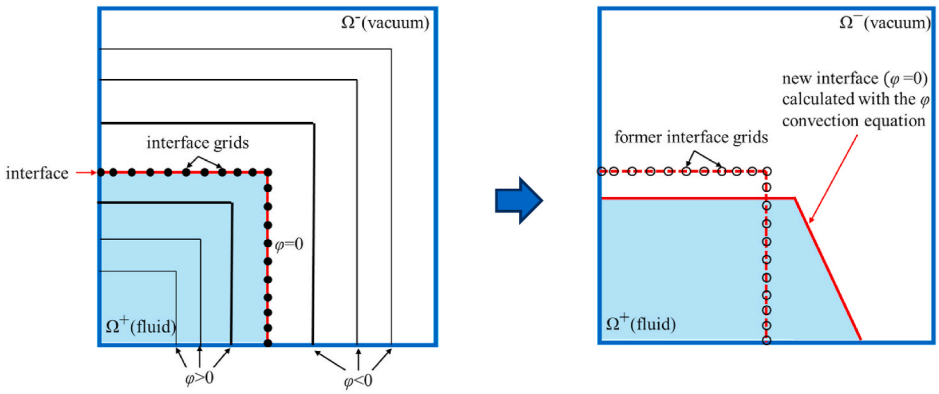

Fig. 10. Level set interface tracking method.

defined by $\varphi < 0$. The motion of the interface where $\varphi = 0$ could be described by the simple convection equation:

$$\frac{\partial \varphi}{\partial t} + v\nabla\varphi = 0 \tag{11}$$

where v represents the velocity of each CFD grid; t is the time. It is a Eulerian formulation of the interface evolution since the interface is captured by the implicit function φ.

For FSI simulation, ALE approach for mesh movement is adopted in the CFD solver, which means that large deformation of the fluid mesh can occur. To maintain the quality of the fluid mesh, an automatic re-meshing is introduced where the solver will use an a-posteriori error estimator to compute a new mesh size to satisfy a maximum perceptual error (Zienkiewicz and Zhu, 1987).

Overall CFD domain at cross section $Y = 0$ is shown in Fig. 11. CFD-FEA coupled simulation can be time-consuming, so it is important to carefully consider the size of the fluid domain. The numerical tank is $4.5L$ in length, $1.2L$ in width and 3 m in depth. Note that the size of the fluid domain is insufficient to be considered a far-field condition. To decrease reflection from the side and outlet boundary, damping zones perpendicular to the side and outlet boundary is created. The damping is achieved by adding a source term S_d to the momentum equations:

$$S_d = \omega_d(f_1 + f_2|u|)u \tag{12}$$

where f_1 and f_2 are damping factor; u is the velocity; ω_d is the weight function:

$$\omega_d = \frac{e^{\varepsilon}\text{-}1}{e\text{-}1} \tag{13}$$

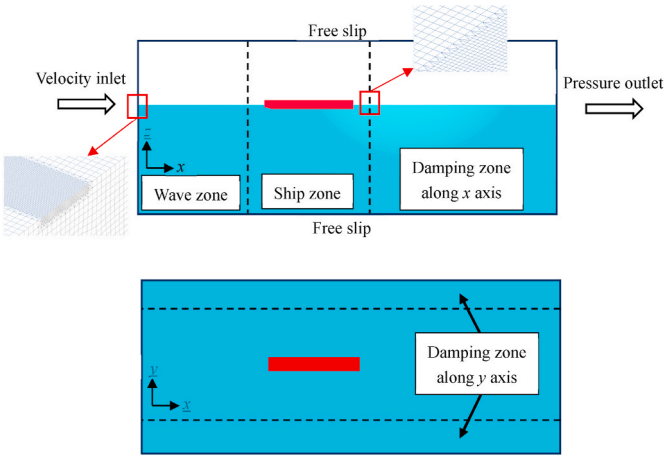

Fig. 11. Overview of CFD domain.

with ε the blending function which allows a smooth insertion of the source term in the damping layer:

$$\varepsilon = \left(\frac{x\text{-}x_{end}}{L_d}\right)^n \tag{14}$$

where x and x_{end} represent the CFD grid coordinates and end coordinates of the damping zone; L_d is the length of the damping zone; n is the scaling factor. In this research, f_1 and f_2 are both set to be 10 while n is set to be 5. The wave inlet boundary of the fluid domain is set to be velocity inlet condition while the wave outlet boundary is set to be pressure outlet condition. The wave model at the inlet is based on the second-order Stokes wave (Whitham, 1974). The bottom and top, as well as side boundary of the fluid domain, are set to be the free-slip conditions. The ship hull is set as a no-slip wall where the fluid tangential velocity is always zero.

The mesh size at the free surface and around the ship hull is refined to capture wave and FSI load properly. A number of 80 cells per wavelength and 20 cells per wave height is recommended by ITTC (ITTC, 2011). In this research tetrahedral mesh is used for CFD simulation. However, controlling the tetrahedral mesh size along a specific direction can be challenging. So, there are three criteria for mesh size: $\lambda/80, B/20, h_0/15$, and the smallest of these is used as the mesh size at the free surface zone. To calculate the FSI load on the hull with high accuracy, the mesh size around the ship hull is the finest over the whole fluid domain. The minimum size of mesh on the ship hull is $\lambda/240$. A total 11.3 million of tetrahedral cells are generated in the fluid domain.

3.3. CFD-FEA two-way coupled method

Typical solutions for FSI problems could be classified into two categories: monolithic approach (Michler et al., 2004) and partitioned approach (Loehner et al., 1998). The CFD-FEA coupled method implemented in LS-DYNA is based on a partitioned approach (Souli and Benson, 2010), where the fluid and solid equations are uncoupled. The partitioned approach relies on finding an approximation of the tangent operator at the FSI interface without having to do a monolithic assembly. The CFD-FEA coupled iteration-resolution scheme is explained in Fig. 12. A strongly coupled partitioned scheme requires the convergence of the fluid and solid variables at the interface and gives the same results as the monolithic scheme after iterative progress. The CFD solver calculates fluid equations first, and then communicates the hydrodynamic forces to the solid mechanical solver. The solid mechanical solver then returns the nodal displacements as boundary conditions for the CFD solver. This procedure is repeated until convergence is reached.

As shown in Fig. 13, the fluid and solid surfaces that will interact in FSI simulation are detected automatically by a criterion, which is the distance d between a CFD grid/FEA node and a FEA element/CFD cell:

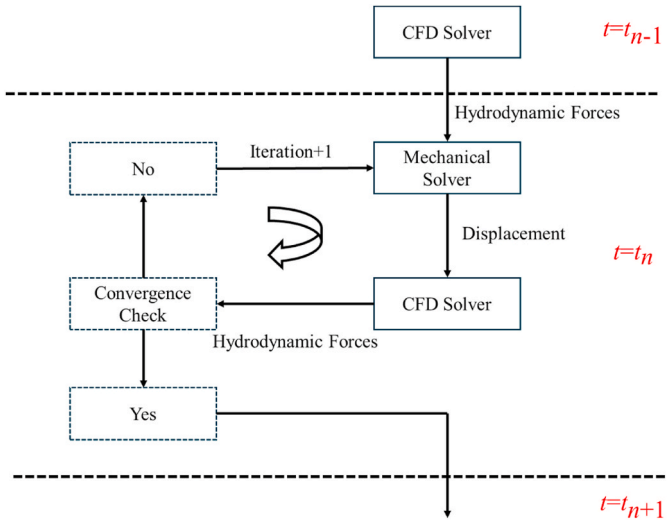

Fig. 12. Strong partitioned iteration-resolution scheme.

$$d \leq IDC \times \min(h, H) \tag{15}$$

where h is the size of the CFD cell; H is the size of the FEA element; IDC is a detection coefficient criterion. In this study, IDC is set to 0.3.

3.4. Numerical hammering test

The natural frequency of a ship structure under dry and wet conditions will be different due to the added mass effect. The added mass effect could be defined as:

$$\omega_{\text{wet}} = \sqrt{\frac{1}{1 + f_{\text{added mass}}}}\omega_{\text{dry}} \tag{16}$$

where ω_{dry} and ω_{wet} represent the dry and wet natural frequencies, respectively; $f_{\text{added mass}}$ is the added-mass factor.

Numerical hammering tests were conducted to determine the natural frequency of the Barge and KVCLL2 structure under dry and wet conditions. An external impulse force, equivalent to the gravitational force of the entire ship, was applied suddenly to the middle of the ship structure (see Fig. 14). Simultaneously, the vertical bending moment (VBM) was measured at the midship.

3.4.1. Damping radio

As mentioned in section 3.1.2, the time integration factors used in FEA simulation were set atypically to enhance the stability of the CFD-FEA coupled simulation. However, this unusual setting may result in unexpected numerical damping. The numerical damping in FEA simulation should be validated by examining the decay of the structural response. The damping ratio is introduced as a criterion, which can be written as:

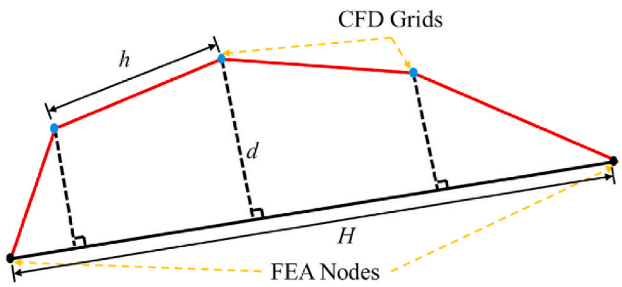

Fig. 13. Detection of the FSI interface.

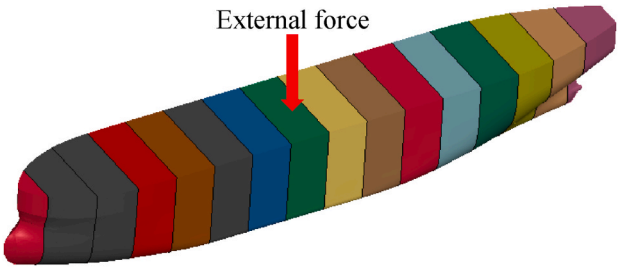

Fig. 14. Applied external force.

$$\zeta = \frac{1}{\sqrt{1 + \left(\frac{2\pi}{\sigma}\right)^2}} \tag{17}$$

where ζ is the damping radio; σ is the logarithmic decrement, the natural log of the ratio of the amplitudes of any two successive peaks, which can be expressed as:

$$\sigma = \frac{1}{n}\ln\frac{x_i}{x_{i+n}} \tag{18}$$

where x_i is the i-th positive peak; x_{i+n} is the $(i + n)$-th positive peak.

As shown in Fig. 15, three different periods of the VBM response are chosen to calculate the damping ratio. The results are shown in Table 7. The damping radio in each period is less than 1% and behaves continuously (at around 0.5%). The time integration factors used in FEA simulation produce a damping ratio within a reasonable range.

3.4.2. Dry condition

At the time instant of 2 s, the external force is applied and the structure starts vibrating. Fig. 16 (b) shows the frequency components of VBM, which are detected by Fast Fourier Transform (FFT) analysis of the measured VBM time series at the midship (see Fig. 16 (a)) The dry natural frequency of the Barge ship can be estimated at 10.5 Hz.

Fig. 17 (a) shows the time history of VBM at the midship of the KVLCC2 ship. Fig. 17 (b) shows the frequency components of VBM, which are also detected by FFT. The dry natural frequency of the KVLCC2 ship can be estimated at 9.1 Hz.

3.4.3. Wet condition

The hammering test under wet condition was performed using two-way coupling between the CFD and FEA models. This is an effective method to measure the wet natural frequency of the FE model (Pal and Iijima, 2022). The fluid domain used for the hammering test is shown in Fig. 18. The external force is applied after confirming the calm water condition. Figs. 19 and 20 show the time history and frequency components of VBM for the Barge and KVLCC2 ship, respectively. The frequency components of VBM are detected by applying the FFT method to the time history of VBM, as in the wet condition.

From Fig. 19 (b) and Fig. 20 (b), the wet natural frequency of the Barge and KVLCC2 ship structure can be estimated at 7.83 Hz and 7.22 Hz. Compared to the dry natural frequency, the wet natural frequency decreases due to the added mass effect of the fluid.

4. Numerical validation

To validate the experimental and numerical model used in this study, the hydroelastic problem of a Barge ship is investigated based on Malenica's model experiment (Senjanović and Malenica, 2003), using the EX-A wave condition for the validation.

Fig. 21 shows the heave RAOs at each monitoring point of the Barge ship under different angular frequencies (ω). The black squares, blue triangles and red circles represent experiment results, Malenica's results

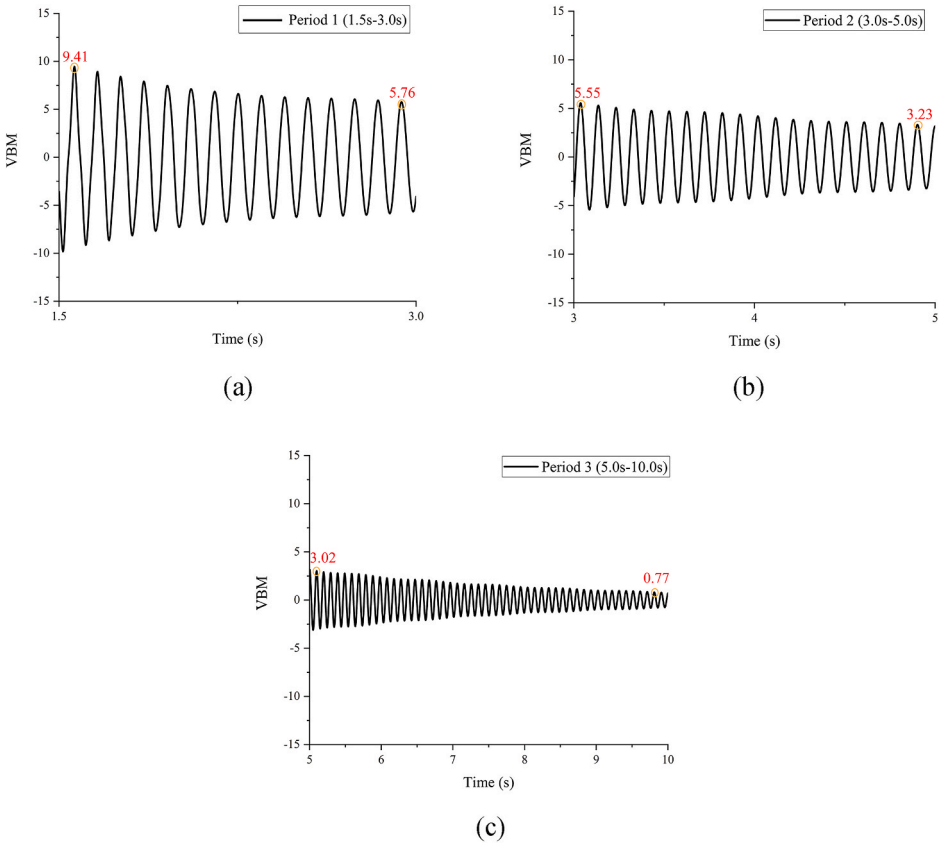

Fig. 15. Decay of VBM in different periods.

Table 7
Damping ratio.

Period	x_i	x_{i+n}	n	ζ
I	9.41	5.76	14	0.56%
II	5.55	3.23	19	0.45%
III	3.02	0.77	49	0.44%
I-III	9.41	0.77	82	0.49%

and the CFD-FEA coupled simulation (LS-DYNA) results, respectively. It can be known from Fig. 21 that the experiment results and the CFD-FEA coupled simulation results both have good agreement with Malenica's results.

Fig. 22 compares the time history of heave motion between the experiment and CFD-FEA coupled simulation. The experimental results are in good agreement with the simulation results. The experimental and numerical methods in this study have been validated.

5. Results and discussion

5.1. Motion response

The comparation of z-displacement RAOs of the Barge ship between the experiment and numerical results are shown in Fig. 23. It can be known from Fig. 23 that the vertical motion response at the bow is the largest; in Fig. 23 (a), (b) and (c), from bow and stern to midship, the vertical motion response gradually reduces. In the range of $\lambda/L_{pp} = 1.0$ to $\lambda/L_{pp} = 1.6$, the vertical motion response has a trend of increase with the augment of λ.

Fig. 24 shows the z-displacement RAOs of the KVLCC2 ship,

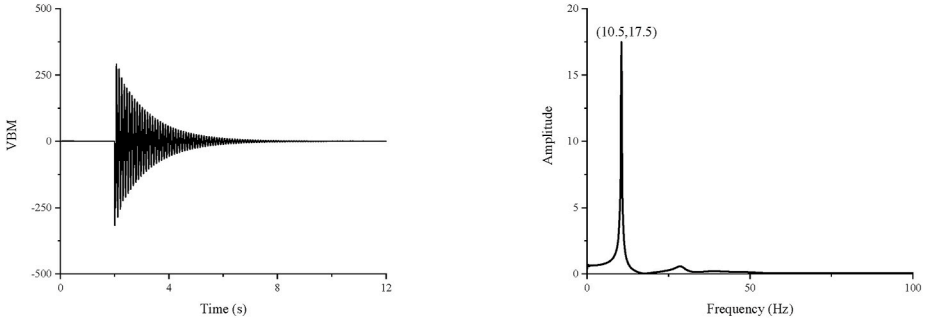

Fig. 16. Time history and frequency components of VBM (Barge ship).

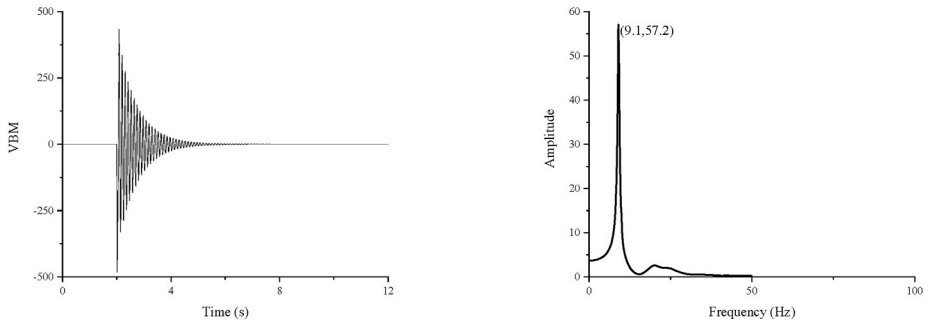

(a) Time history of VBM (b) Frequency components of VBM

Fig. 17. Time history and frequency components of VBM (KVLCC2 ship).

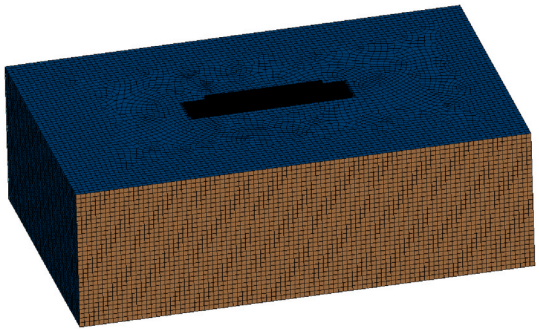

Fig. 18. Fluid domain for hammering test under wet condition.

comparing the results of the experiment and numerical simulation. The numerical results have good agreement with experiment results except for the midship region. At the midship, the numerical result in every case is obviously less than the experiment result. The difference between the numerical model (continuous model) and the experimental model (segmented model) is the reason for this. For the continuous model, all parts of the ship move together and both sides of the ship will have a larger influence on the movement at the midship. Hence, this difference between numerical and experiment results at midship is reasonable. From Fig. 24, the minimum heave RAO can be observed around the midship. The displacement RAO increases from the midship to the bow and stern. The vibration mode of the ship is mainly a 2-node model. When wavelength grows (from C3 to C5), the vertical motion response has a trend of increment with the augment of λ.

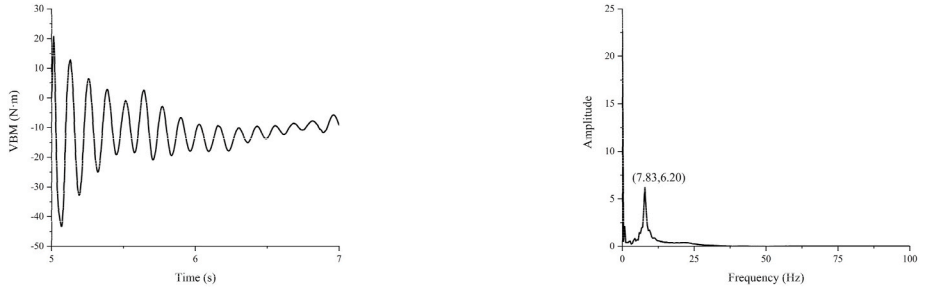

(a) Time history of VBM (b) Frequency components of VBM

Fig. 19. Time history and frequency components of VBM (Barge ship).

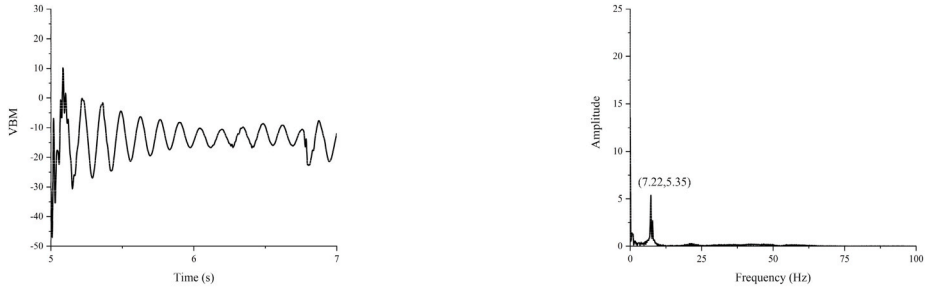

(a) Time history of VBM (b) Frequency components of VBM

Fig. 20. Time history and frequency components of VBM (KVLCC2 ship).

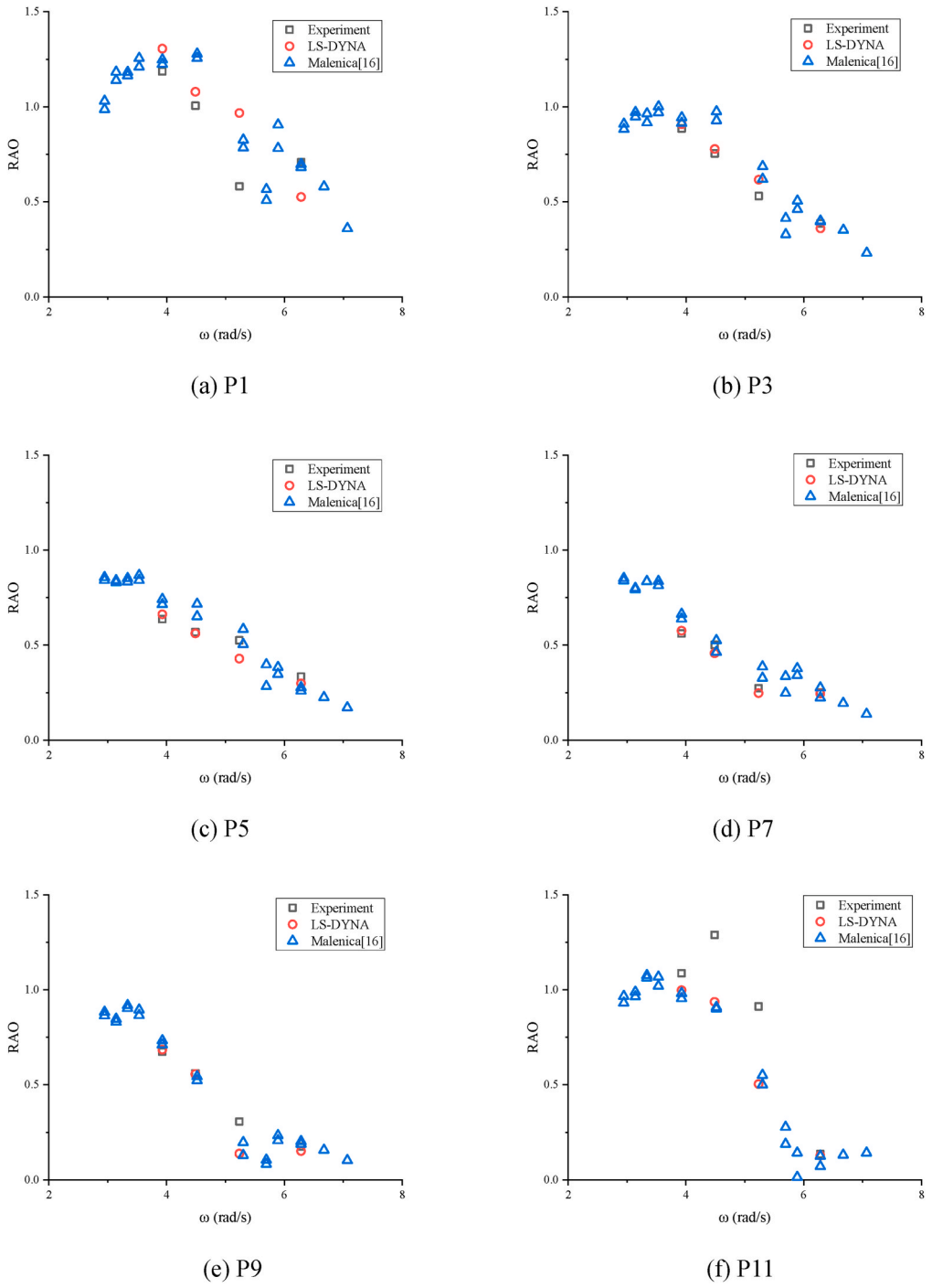

Fig. 21. Comparation of heave RAOs.

5.2. Wave-induced VBM

5.2.1. Frequency components of VBM

As wave induced VBM usually contains wave frequency (WF) components and high frequency (HF) components, the FFT is used to transfer time history results into frequency components. Fig. 25 shows the frequency components of VBM under typical wave conditions for the Barge ship. The structure is primarily exited by the wave frequency, and the WF component matches well with the frequency of the incident wave.

The frequency components of VBM of the KVLCC2 under the C3 condition are shown in Fig. 26. It is clear that the WF component as well as the higher-order harmonics are observed. The peak of the WF and 2-node high frequency (HF) component is higher than other harmonic components.

An FFT band-pass filter is used to divide the VBM into different frequency components, including the WF, 2nd to higher springing harmonic orders harmonics. Some of these different frequency components are shown in Fig. 27. The frequency range of each component is also shown in the figure. All the frequency components in Fig. 27 have good agreement with the sinusoidal shape. The WF and 2-node HF response are significantly higher than other harmonic components.

5.2.2. Time history of VBM at the WF

As discussed in the previous section, the wave-induced VBM usually

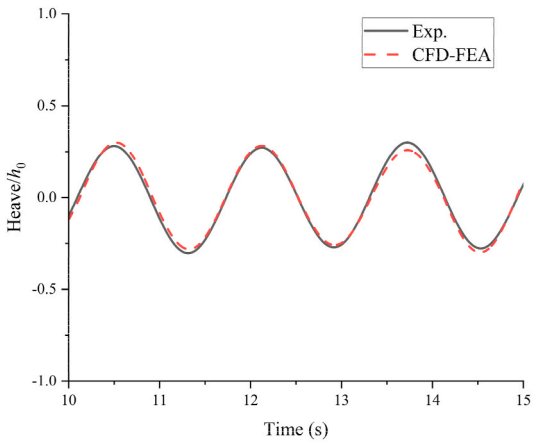

(a) A1 (λ=3.996m)

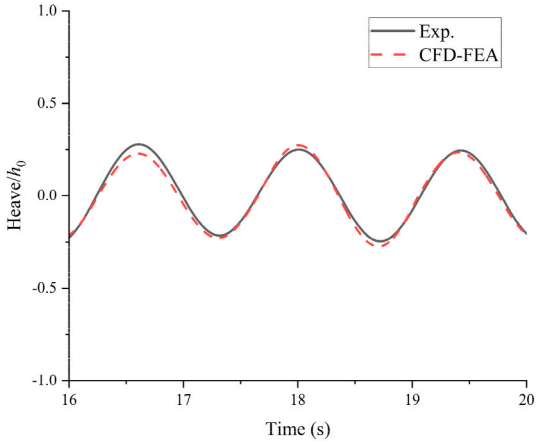

(b) A2 (λ=3.063m)

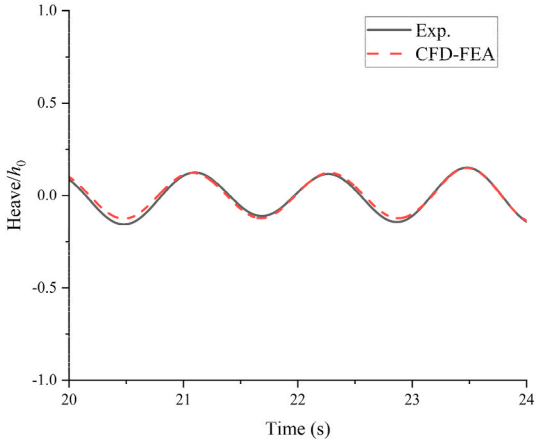

(c) A3 (λ=2.248m)

Fig. 22. Comparation of heave motion.

contains the WF and HF components. However, HF components are not the focus of this study. The structure response excited by wave frequency will be discussed in this section. Hence, the FFT filter is adopted to obtain the WF components in VBM. The cut-off frequency used here is

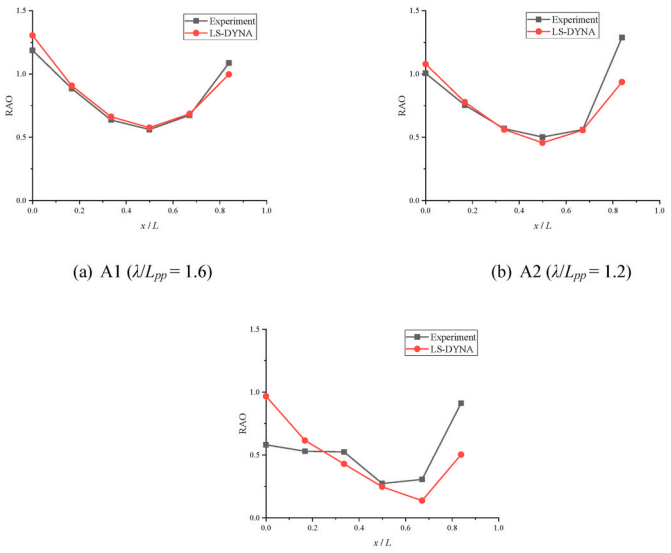

(a) A1 (λ/L_{pp} = 1.6) (b) A2 (λ/L_{pp} = 1.2)

(c) A3 (λ/L_{pp} = 1.0)

Fig. 23. The z-displacement RAO under different wave conditions (Barge ship).

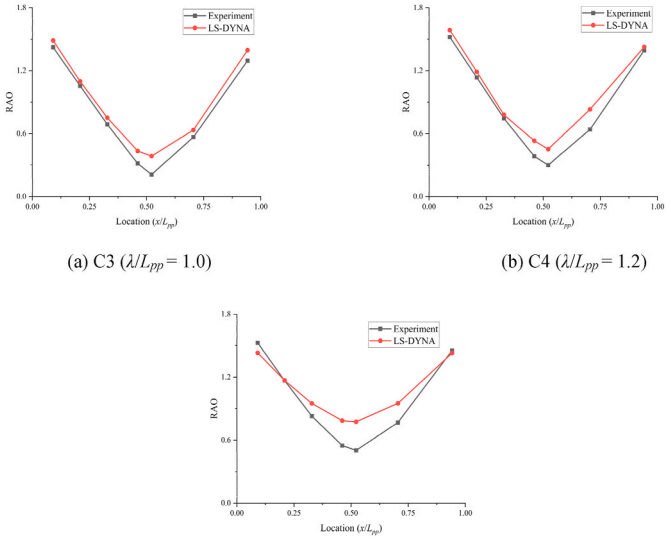

(a) C3 (λ/L_{pp} = 1.0) (b) C4 (λ/L_{pp} = 1.2)

(c) C5 (λ/L_{pp} = 1.5)

Fig. 24. The z-displacement RAO under different wave conditions (KVLCC2 ship).

1.1 Hz.

Fig. 28 illustrates a comparison of VBM at the middle of the Barge ship among three typical wave conditions. The black, red, and blue curves represent A1 - A3 wave conditions, respectively. As the wave height of each wave condition remains constant, the VBMs caused by different wave conditions are within a similar range. However, it can be seen from Fig. 28 that the VBM has a trend of decreasing with the decrement of wavelength.

The time history of VBM at the middle of the KVLCC2 ship is shown in Fig. 29 under typical wave conditions The black curve, red curve and blue curve represent C3 – C5 wave conditions, respectively. Similar to the result of the Barge ship, the VBMs caused by different wave conditions are within a similar range. The same trend of VBM can also be observed from Fig. 29.

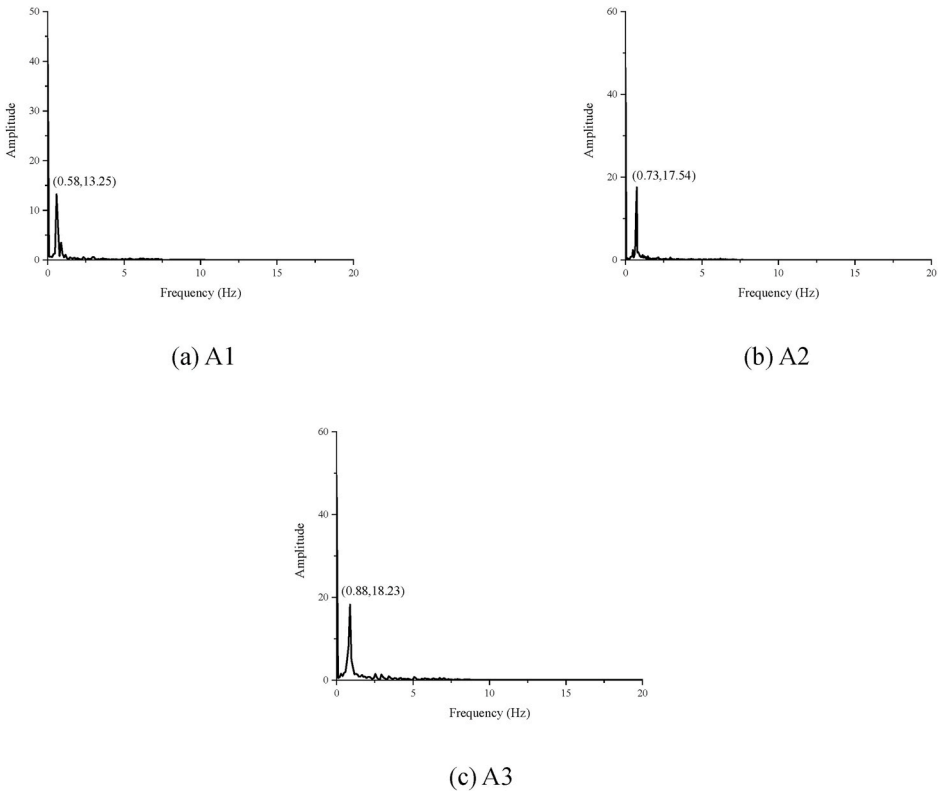

Fig. 25. Frequency components of VBM under typical wave conditions (Barge ship).

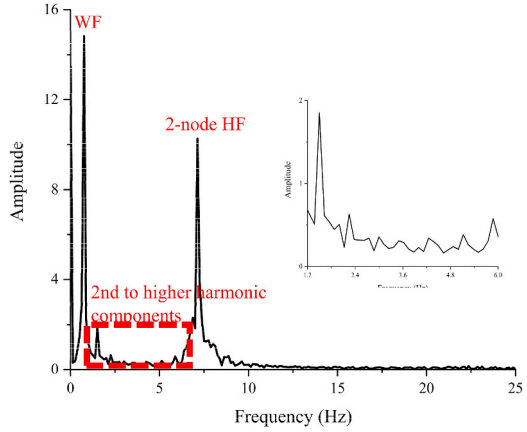

Fig. 26. Frequency components of VBM at $\lambda/L_{pp} = 1.0$ (KVLCC2 ship).

6. Conclusions

This paper investigated the hydroelastic response of a Barge and KVLCC2 model under different wave conditions using experimental analysis and strongly coupled two-way CFD-FEA method. By comparing numerical prediction results and tank test results of the Barge ship with published results, the experimental analysis and numerical methods were validated. By analyzing motion and VBM of the ship, conclusions can be summarized as follows.

(1) The strongly coupled two-way CFD-FEA method used in this study shows good accuracy in simulating ship-wave interaction problems. Nonlinearity combined with both fluid and structure can be calculated with high stability using this method.

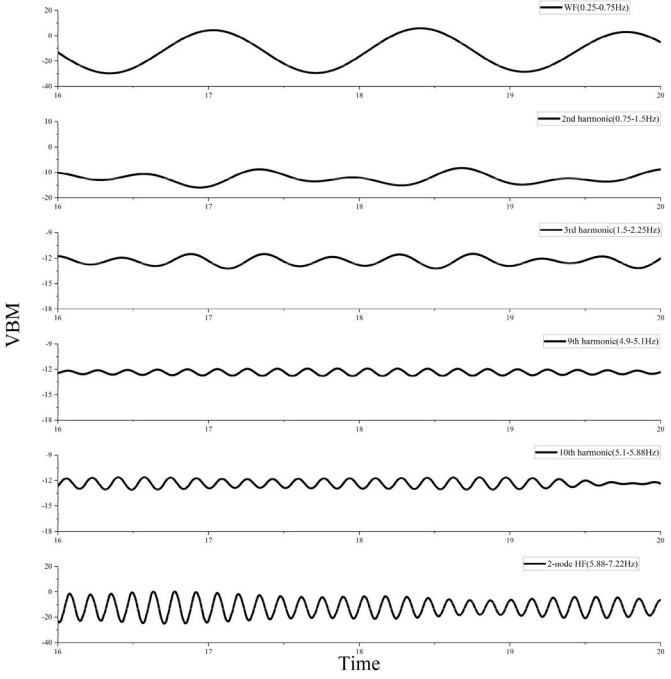

Fig. 27. Time history of VBM with different frequency at $\lambda/L_{pp} = 1.0$ (KVLCC2 ship).

(2) The response of vertical displacement RAOs indicates that the ship structure is primarily in 2-node mode under various wave conditions in this study. At the midship, the simulation results of the KVLCC2 ship are larger than the experimental results due to differences in the models used, specifically the continuous and segmented models.

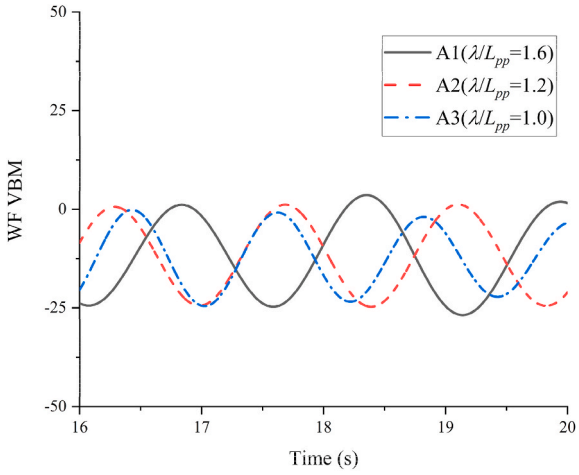

Fig. 28. Comparation of VBM at the midship under typical wave conditions (Barge ship).

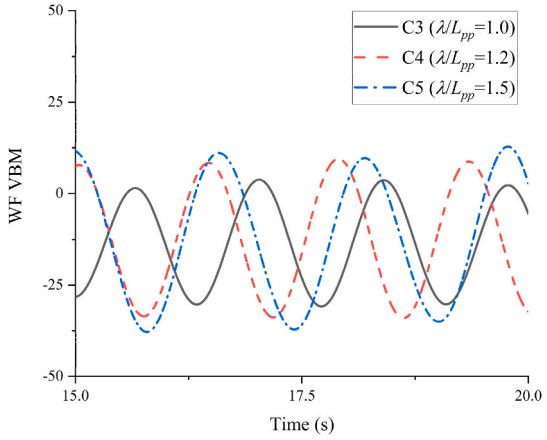

Fig. 29. Comparation of VBM at midship under typical wave conditions (KVLCC2).

(3) The structural response was discussed in terms of midship VBM. The VBM has a tendency to decrease with decreasing wavelength. Meanwhile, the high-order harmonics of VBM response are observed through the FFT analysis. Further investigation on this is needed.

In the future, investigation of the hydroelastic response of ships with various forward speeds and heading angles under regular and irregular waves using the CFD-FEA coupled method will be meaningful and interesting. Meanwhile, the higher-order components observed in the CFD-FEA coupled simulation may need further investigation.

CRediT authorship contribution statement

Binyang Xie: Writing – original draft, Software, Methodology, Formal analysis, Data curation. **Guanghua He:** Writing – review & editing, Supervision, Resources, Conceptualization. **Chuankai Zhao:** Writing – review & editing, Validation, Methodology. **Penglin Jing:** Writing – review & editing, Validation, Methodology. **Sumit Kumar Pal:** Writing – review & editing, Methodology, Data curation. **Kazuhiro Iijima:** Writing – review & editing, Software, Methodology. **Ruijia Jin:** Resources, Methodology. **Bangqi Chen:** Supervision, Formal analysis. **Hassan Ghassemi:** Writing – review & editing, Supervision.

Declaration of competing interest

The authors declare that they have no known competing financial interests or personal relationships that could have appeared to influence the work reported in this paper.

Data availability

Data will be made available on request.

Acknowledgements

This work is supported by the Taishan Scholars Project of Shandong Province (tsqn201909172), Fundamental Research Funds for the Central Universities (HIT.OCEF. 2021037), University Young Innovational Team Program, Shandong Province (2019KJN003).

References

Bales, S.L., 1983. Designing SHIPS TO the natural environment. Nav. Eng. J. 95, 31–40. https://doi.org/10.1111/j.1559-3584.1983.tb00574.x.
Bathe, K.-J., 2007. Conserving energy and momentum in nonlinear dynamics: a simple implicit time integration scheme. Comput. Struct. 85, 437–445. https://doi.org/10.1016/j.compstruc.2006.09.004.
Bathe, K.-J., Noh, G., 2012. Insight into an implicit time integration scheme for structural dynamics. Comput. Struct. 98–99, 1–6. https://doi.org/10.1016/j.compstruc.2012.01.009.
Bishop, R.E.D., Price, W.G., 1983. An introduction to ship hydroelasticity. J. Sound Vib. 87, 391–407. https://doi.org/10.1016/0022-460X(83)90469-8.
Bishop, R.E.D., Price, W.G., 1979. Hydroelasticity of Ships. Cambridge University Press, Cambridge [Eng.] ; New York.
Bishop, R.E.D., Price, W.G., Wu, Y., 1986. A general linear hydroelasticity theory of floating structures moving in a seaway. Philos. Trans. R. Soc. Lond. Ser. Math. Phys. Sci. 316, 375–426. https://doi.org/10.1098/rsta.1986.0016.
Brown, D.L., Cortez, R., Minion, M.L., 2001. Accurate projection methods for the incompressible Navier–Stokes equations. J. Comput. Phys. 168, 464–499. https://doi.org/10.1006/jcph.2001.6715.
Chen, X., Wu, Y., Cui, W., Tang, X., 2003. Nonlinear hydroelastic analysis of a moored floating body. Ocean Eng 30, 965–1003. https://doi.org/10.1016/S0029-8018(02)00078-1.
Chen, Z., Jiao, J., Li, H., 2017. Time-domain numerical and segmented ship model experimental analyses of hydroelastic responses of a large container ship in oblique regular waves. Appl. Ocean Res. 67, 78–93. https://doi.org/10.1016/j.apor.2017.07.005.
Class, N.K., 2014. Investigation Report on Structural Safety of Large Container Ships. Class NK.
Fonseca, N., Guedes Soares, C., 2004. Experimental investigation of the nonlinear effects on the statistics of vertical motions and loads of a containership in irregular waves. J. Ship Res. 48, 148–167. https://doi.org/10.5957/jsr.2004.48.2.148.
Fu, S., Moan, T., Chen, X., Cui, W., 2007. Hydroelastic analysis of flexible floating interconnected structures. Ocean Eng 34, 1516–1531. https://doi.org/10.1016/j.oceaneng.2007.01.003.
Guo, H., Zou, Z., 2017. System-based investigation on 4-DOF ship maneuvering with hydrodynamic derivatives determined by RANS simulation of captive model tests. Appl. Ocean Res. 68, 11–25. https://doi.org/10.1016/j.apor.2017.08.006.
He, G., Kashiwagi, M., 2012. Numerical analysis of the hydroelastic behavior of a vertical plate due to solitary waves. J. Mar. Sci. Technol. 17, 154–167. https://doi.org/10.1007/s00773-011-0155-9.
Iijima, K., Hermundstad, O.A., Zhu, S., Moan, T., 2009. Symmetric and Antisymmetric Vibrations of a Hydroelastically Scaled Model. In: Presented at the Proc. Hydroelasticity in Marine Technology. University of Southampton, UK, pp. 173–182.
Iijima, K., Yao, T., Moan, T., 2008. Structural response of a ship in severe seas considering global hydroelastic vibrations. Mar. Struct. 21, 420–445. https://doi.org/10.1016/j.marstruc.2008.03.003.
ITTC, 2011. Recommended Procedures and Guidelines: Practical Guidelines for Ship CFD Applications.
Jiao, J., Yu, H., Chen, C., Ren, H., 2019. Time-domain numerical and segmented model experimental study on ship hydroelastic responses and whipping loads in harsh irregular seaways. Ocean Eng 185, 59–81. https://doi.org/10.1016/j.oceaneng.2019.05.039.
Jiao, J., Zhao, Y., Ai, Y., Chen, C., Fan, T., 2018. Theoretical and experimental study on nonlinear hydroelastic responses and slamming loads of ship advancing in regular waves. Shock Vib. 2018, 1–26. https://doi.org/10.1155/2018/2613832.
Kim, Y., Kim, B.-H., Choi, B.-K., Park, S.-G., Malenica, S., 2018. Analysis on the full scale measurement data of 9400TEU container Carrier with hydroelastic response. Mar. Struct. 61, 25–45. https://doi.org/10.1016/j.marstruc.2018.04.009.
Kim, Yooil, Kim, K.-H., Kim, Yonghwan, 2009. Analysis of hydroelasticity of floating shiplike structure in time domain using a fully coupled hybrid BEM-FEM. J. Ship Res. 53, 31–47. https://doi.org/10.5957/jsr.2009.53.1.31.

Korobkin, A., Părău, E.I., Vanden-Broeck, J.-M., 2011. The mathematical challenges and modelling of hydroelasticity. Philos. Trans. R. Soc. Math. Phys. Eng. Sci. 369, 2803–2812. https://doi.org/10.1098/rsta.2011.0116.

Lee, K.-H., Lee, P.-S., 2016. Nonlinear hydrostatic analysis of flexible floating structures. Appl. Ocean Res. 59, 165–182. https://doi.org/10.1016/j.apor.2016.05.016.

Lee, Y., Wang, Z., White, N., Hirdaris, S.E., 2011. Time Domain Analysis of Springing and Whipping Responses Acting on a Large Container Ship. In: Volume 6: Ocean Engineering. Presented at the ASME 2011 30th International Conference on Ocean, Offshore and Arctic Engineering. ASMEDC, Rotterdam, The Netherlands, pp. 139–147. https://doi.org/10.1115/OMAE2011-49218.

Loehner, R., Yang, C., Cerbal, J., Baum, J., Luo, H., Pelessone, D., Charman, C., 1998. Fluid-structure-thermal Interaction Using a Loose Coupling Algorithm and Adaptive Unstructured Grids. In: 29th AIAA, Fluid Dynamics Conference. Presented at the 29th AIAA, Fluid Dynamics Conference. American Institute of Aeronautics and Astronautics, Albuquerque,NM,U.S.A. https://doi.org/10.2514/6.1998-2419.

Lu, Y., Liu, W., Zou, Q., Zhang, Y., Qu, H., Song, X., 2024. Hydroelasto-plastic experiment and numerical investigation on a three-cabin ship model in waves. Appl. Ocean Res. 145, 103901 https://doi.org/10.1016/j.apor.2024.103901.

Malenica, Š., Korobkin, A.A., Scolan, Y.-M., Gueret, R., Gazzola, T., Mravak, Z., Chen, X. B., 2006. Hydroelastic Impacts in the Tanks of LNG Carriers. In: Presented at the 4th International Conference on Hydroelasticity in Marine Technology, Wuxi, China, pp. 1–4.

Michler, C., Hulshoff, S.J., Van Brummelen, E.H., De Borst, R., 2004. A monolithic approach to fluid–structure interaction. Comput. Fluids 33, 839–848. https://doi.org/10.1016/j.compfluid.2003.06.006.

Newmark, N.M., 1959. A method of computation for structural dynamics. J. Eng. Mech. Div. 85, 67–94. https://doi.org/10.1061/JMCEA3.0000098.

Osher, S., Fedkiw, R., Piechor, K., 2004. Level set methods and dynamic implicit surfaces. Appl. Mech. Rev. 57, B15. https://doi.org/10.1115/1.1760520.

Pal, S.K., Iijima, K., 2022. Investigation of Springing Responses to High Harmonics of Wave Loads by Direct Coupling between CFD and FEM. In: Volume 7: CFD and FSI. Presented at the ASME 2022 41st International Conference on Ocean, Offshore and Arctic Engineering. American Society of Mechanical Engineers, Hamburg, Germany. https://doi.org/10.1115/OMAE2022-79446. V007T08A043.

Pal, S.K., Xie, B., Iijima, K., Fujikubo, M., 2023. Hull Girder Collapse Analysis in Extreme Wave by Direct Coupled Simulation between CFD and FEM. In: Advances in the Analysis and Design of Marine Structures. CRC Press.

Price, W.G., 1985. Structural Responses of a SWATH or Multi-Hulled Vessel Traveling in Waves. In: Presented at the International Conference on SWATH Ships and Advanced Multi-Hulled Vessels. RINA, London.

Remy, F., Molin, B., Ledoux, A., 2006. Experimental and Numerical Study of the Wave Response of a Flexible Barge. In: Presented at the 4th International Conference on Hydroelasticity in Marine Technology, Wuxi, China.

Riggs, H.R., Niimi, K.M., Huang, L.L., 2007. Two benchmark problems for three-dimensional, linear hydroelasticity. J. Offshore Mech. Arctic Eng. 129, 149–157. https://doi.org/10.1115/1.2746397.

Senjanović, I., Malenica, Š., 2003. Hydroelastic response of a barge to impulsive and non-impulsive wave loads. Int. Conf. Hydroelasticity Mar. Technol. 3, 107–115.

Souli, M., Benson, D.J. (Eds.), 2010. Arbitrary Lagrangian-Eulerian and Fluid-Structure Interaction: Numerical Simulation. ISTE. Wiley, London, Hoboken, NJ.

Southall, N., Sangkyu, Choi, Yongwon, Lee, Chunbeom, H., Hirdaris, S., White, N., 2015. Impact analysis using CFD – a comparative study. https://doi.org/10.13140/RG.2.1.4831.8805.

Wei, Y., Incecik, A., Tezdogan, T., 2023. A hydroelasticity analysis of a damaged ship based on a two-way coupled CFD-DMB method. Ocean Eng 274, 114075. https://doi.org/10.1016/j.oceaneng.2023.114075.

Wei, Y., Yu, S., Jin, P., Huang, L., Elsherbiny, K., Tezdogan, T., 2024. Coupled analysis between catenary mooring and VLFS with structural hydroelasticity in waves. Mar. Struct. 93, 103516 https://doi.org/10.1016/j.marstruc.2023.103516.

Whitham, G.B., 1974. Linear and Nonlinear Waves, Pure and Applied Mathematics. Wiley, New York.

Wu, Y., 1984. Hydroelasticity of Floating Bodies. Brunel University, London.

Wu, Y.S., Tian, C., 2008. Review of research on the hydroelasticity of ship. Shipbuild. China 49, 1–11.

Xia, J., Wang, Z., Jensen, J.J., 1998. Non-linear wave loads and ship responses by a time-domain strip theory. Mar. Struct. 11, 101–123. https://doi.org/10.1016/S0951-8339(98)00008-2.

Yang, P., Feng, Q., Chen, H., Wen, L., 2021. Combined backbone application on numerical simulations and a model experiment of a 20,000 TEU container ship. Ocean Eng 223, 108662. https://doi.org/10.1016/j.oceaneng.2021.108662.

Zhang, X., Gu, X., Ma, N., 2019. Prediction of roll hydrodynamic characteristics for a ship hull section with a high-order finite volume solver. Ocean Eng 180, 119–129. https://doi.org/10.1016/j.oceaneng.2019.04.012.

Zhu, S., Wu, M., Moan, T., 2011a. Experimental and numerical study of wave-induced load effects of open ships in oblique seas. J. Ship Res. 55, 100–123. https://doi.org/10.5957/jsr.2011.55.2.100.

Zhu, S., Wu, M., Moan, T., 2011b. Experimental investigation of hull girder vibrations of a flexible backbone model in bending and torsion. Appl. Ocean Res. 33, 252–274. https://doi.org/10.1016/j.apor.2011.08.001.

Zienkiewicz, O.C., Zhu, J.Z., 1987. A simple error estimator and adaptive procedure for practical engineerng analysis. Int. J. Numer. Methods Eng. 24, 337–357. https://doi.org/10.1002/nme.1620240206.